GEOLOGY | THE GEOLOGICAL SOCIETY OF AMERICA®

https://doi.org/10.1130/G49888.1

Manuscript received 13 September 2021
Revised manuscript received 19 November 2021
Manuscript accepted 20 December 2021

Published online 24 March 2022

Nanoscale isotopic evidence resolves origins of giant Carlin-type ore deposits

E.A. Holley[1]*, A. Fulton[1], C. Jilly-Rehak[2,3†], C. Johnson[4†] and M. Pribil[4†]

[1]Mining Engineering, Colorado School of Mines, 1600 Illinois Street, Golden, Colorado 80401, UA
[2]Department of Geological Sciences, Stanford University, 367 Panama Mall, Stanford, California 94305, USA
[3]Stanford Nano Shared Facilities, Stanford University, 348 Via Pueblo, Stanford, California 94305, USA
[4]U.S. Geological Survey, Geology, Geochemistry, and Geophysics Science Center, Denver Federal Center, Denver, Colorado 80225, USA

ABSTRACT

The western North American Great Basin's Carlin-type deposits represent the largest accumulation of gold in the Northern Hemisphere. The controversy over their origins echoes the debate between Neptunists and Plutonists at the birth of modern geology: were the causative processes meteoric or magmatic? Sulfur isotopes have long been considered key to decoding metal cycling in the Earth's crust, but previous studies of Carlin-type pyrite lacked the spatial resolution to quantify differences among the numerous generations of sulfide mineralization. We developed a new dual-method, nanoscale approach to examine the fine-grained ore pyrite. The $\delta^{34}S$ of the ore pyrite varies systematically with Au concentration at the nanoscale, indicating that both magmatic and meteoric fluids contributed during mineralization, but the magmas brought the gold. Repeated oscillations in fluid ratios upgraded the metal content, resulting in high gold endowment. Our results demonstrate that high-spatial-resolution studies are key to elucidate the spatiotemporal evolution of complex hydrothermal systems.

INTRODUCTION

The Carlin-type gold deposits in the Great Basin (western North America; Fig. 1) are the largest accumulations of gold and the least understood gold deposit type in the Northern Hemisphere, inspiring questions about the processes governing metal cycling and mineralization in the Earth's crust. More gold is produced annually from these deposits than from any other site in the world (Harper, 2020). Carlin-type deposits also represent potential resources of "critical minerals", including arsenic and antimony (Goldfarb et al., 2016). Carlin-type ore occurs as disseminated hydrothermal replacement bodies, primarily hosted in structures crosscutting decarbonated silty limestones. The gold exists in solid solution or as nanoparticles within micron- to nanometer-thick rims of hydrothermal arsenian pyrite overgrowing older sedimentary and magmatic-hydrothermal pyrite grains that were present in the host rocks prior to gold mineralization. Although deposits with similar characteristics occur elsewhere on the planet, it has been suggested that the enormous gold endowment in the Great Basin represents a nonreplicable combination of geologic processes (Cline et al., 2005). The source of Carlin-type gold has eluded definition, echoing the debate waged between neptunists and plutonists at the birth of modern geology: Did meteoric fluids scavenge and then redeposit gold as they circulated through the sedimentary rocks (Ilchik and Barton, 1997; Emsbo et al., 2003; Large et al., 2011), or was the gold introduced by magmas (Sillitoe and Bonham, 1990; Ressel and Henry, 2006; Muntean et al., 2011)?

Carlin-type deposits are notoriously difficult to study because their mineralogy is not amenable to the traditional tools used to fingerprint the origins of metal enrichment (Richards, 2011). Fine-scale zonation in sulfide mineral geochemistry is common in many deposit styles, and the spatial resolution of traditional analytical techniques has been insufficient to differentiate among Carlin-type pyrite generations. Hydrogen and oxygen isotopes of the clays and fluid inclusions at Carlin-type deposits represent mixtures between syn-ore and pre-ore phases, consistent with precipitation from a meteoric fluid or mixing between meteoric and magmatic fluids (Hofstra and Cline, 2000; Cline et al., 2005, and references therein). Carlin-type mineralization ages are imperfectly constrained due to the paucity of dateable syn-ore minerals, but the timing of mineralization appears to track the late Eocene southwestern sweep of calc-alkaline magmatism through the region (Cline et al., 2005). Several Carlin-type gold districts in the Great Basin show no evidence of Eocene magmatism (Fig. 1), and the sedimentary host rocks are unusually enriched in metals including Au and As (Emsbo et al., 2003; Large et al., 2009). Similar smaller deposits elsewhere in the world lack evidence for syn-mineralization magmatism (Cline, 2018; Pinet et al., 2020).

Because reduced sulfur served as the principal ligand during gold transport (Cline et al., 2005), sulfur isotopes have long been considered the unattainable key to determine the origins of Carlin-type gold (gold itself has only one stable isotope). The term "$\delta^{34}S$" refers to the isotope ratio $^{34}S/^{32}S$ (‰) relative to Vienna Cañon Diablo troilite. The $\delta^{34}S$ values of ore pyrite can be compared to the $\delta^{34}S$ of potential sulfur reservoirs. Elemental analyzer–isotope ratio mass spectrometry (EA-IRMS) of whole grains gives $\delta^{34}S$ values that average the older pyrite and hydrothermal pyrite overgrowths; results are permissive of either magmatic or sedimentary origins (Cline et al., 2005; Christiansen et al., 2011). Traditional secondary ion mass spectrometry (SIMS) studies reached varying conclusions based on only a few data points from spot sizes of 10–30 μm encompassing multiple compositional zones in the pyrite. Data are suggestive of a magmatic origin at Getchell and Betze-Post (Nevada, USA; Cline et al., 2003; Kesler et al., 2003; Henkelman, 2004; Kesler et al., 2005). Relative differences in $^{34}S/^{32}S$ between cores

*E-mail: eholley@mines.edu
†These authors contributed equally to this work.

CITATION: Holley, E.A., et al., 2022, Nanoscale isotopic evidence resolves origins of giant Carlin-type ore deposits: Geology, v. XX, p. , https://doi.org/10.1130/G49888.1

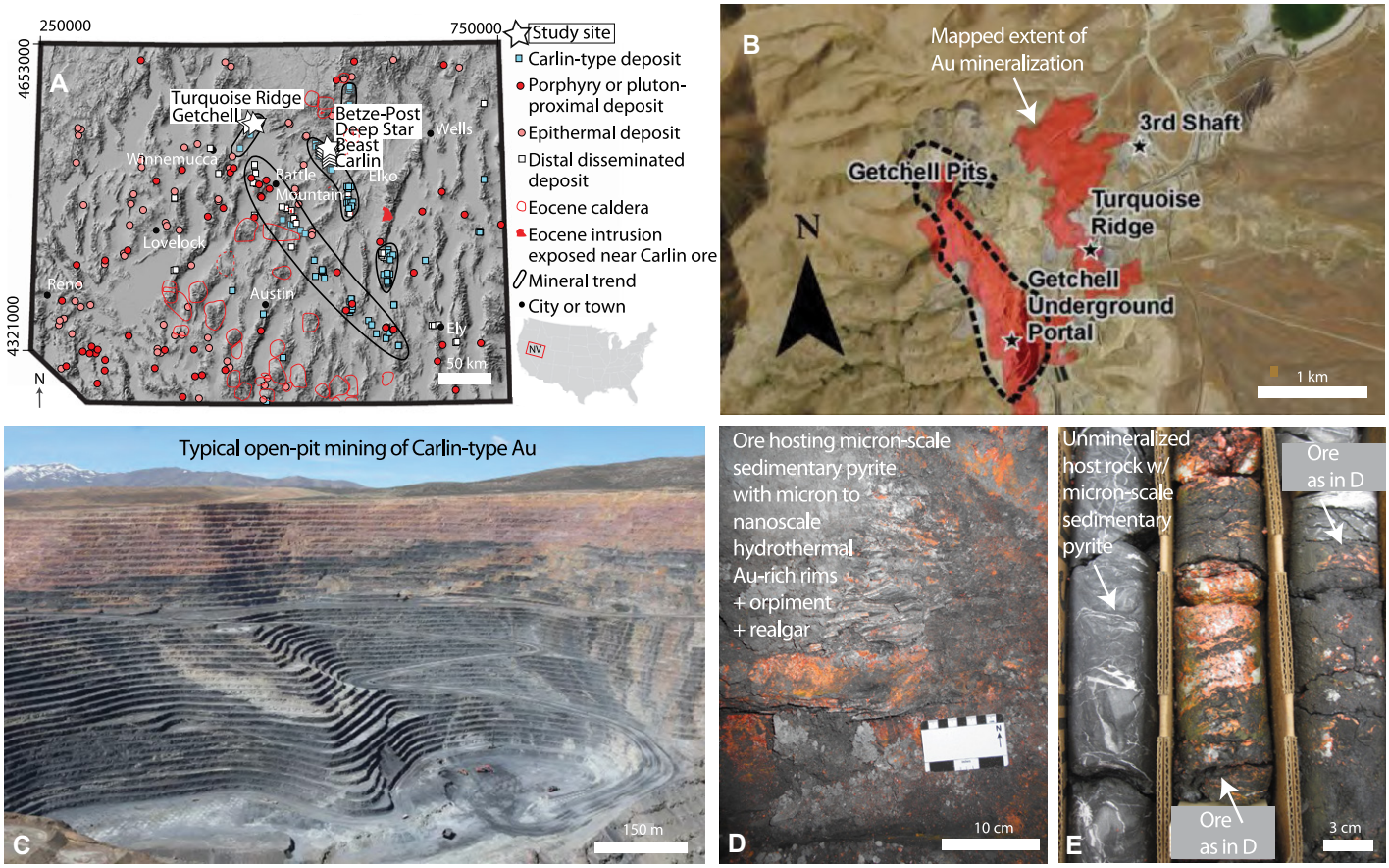

Figure 1. Carlin-type deposits across scales. (A) Carlin-type and known magmatic-hydrothermal ore deposits in northern Nevada, USA; not all Carlin-type deposits are located near known Eocene intrusions (data from Wallace et al., 2004; Henry and John, 2013; Holley et al., 2019; Henry et al., 2021). NV—Nevada. Relief map of topography is from Wallace et al. (2004). Coordinate system is UTM. (B) Mapped extent of mineralization at Turquoise Ridge and Getchell. Base imagery is from Nevada Gold Mines (2021). (C) Open-pit mining of Carlin-type ore at Twin Creeks northeast of Turquoise Ridge (Nevada Gold Mines, 2021). (D,E) Underground mine exposure (D) and drill core (E) at Turquoise Ridge.

and rims were determined for three grains from Turquoise Ridge and West Banshee using qualitative nanoscale SIMS (NanoSIMS) mapping (Barker et al., 2009) and atom probe tomography (Gopon et al., 2019), but the data were not standardized so the origins of the gold-bearing fluid remained elusive. We paired NanoSIMS depth profiles and laser ablation–multicollector–inductively coupled plasma mass spectrometry (LA-MC-ICPMS) to resolve the insufficient spatial resolution and the potential for matrix effects inherent in previous methods.

MATERIALS AND METHODS

We examined ore pyrites in 40 samples from five well-studied Carlin-type deposits in Nevada—Carlin, Deep Star, Beast, Turquoise Ridge, and Getchell—as well as northern Carlin-trend Eocene dikes (Fig. 1; see the Supplemental Material[1]). From petrography and scanning electron microscopy of thousands of pyrite grains, we selected 64 locations in representative grains for *in situ* sulfur isotopic and trace element study. We made NanoSIMS maps of the grains by collecting ^{63}Cu, ^{75}As, ^{107}Ag, ^{117}Sb, and ^{197}Au data on electron multipliers and calibrated the data with relative sensitivity factors using an electron microprobe. Figure 2 shows representative examples of the target locations and NanoSIMS maps.

Standardized, quantitative analyses of sulfur isotopes in sulfide minerals were previously only possible at a spatial resolution of 1–15 μm (Zhang et al., 2014, 2017; Hauri et al., 2016). The methods ignored compositional heterogeneity in the *Z*-direction, averaging NanoSIMS data over the length of an entire analytical run. We improved the method to record nanoscale compositional variation by producing a depth profile at each of our 64 spots, gathering 2400 individual data points per analytical run as the beam penetrated through successive heterogeneous geochemical zones (see the Supplemental Material). Each depth-profile data point represents a depth interval of <1 nm. Figure 3 shows six representative depth profiles. To quantify trends in a manageably reduced number of data points, we calculated plateau averages from zones of consistent composition within each depth profile (see the Supplemental Material). In Figures 4A–4D and in Table S1 (in the Supplemental Material), we present data for 89 NanoSIMS plateaus. The average $\delta^{34}S$ ratio error for plateaus was ±0.86 (one standard deviation) (Table S1). We validated our NanoSIMS results from coarse areas using 5 μm LA-MC-ICPMS spots in 23 locations. The $\delta^{34}S$ data are consistent between the two methods (Table S2), indicating that our observed core-rim fractionations are not due to matrix effects.

RESULTS

Ore Pyrite $\delta^{34}S$ Varies Systematically with Au

The pre-mineralization sedimentary pyrite at Carlin, Getchell, and Turquoise Ridge contains little Au or As (Figs. 2 and 3A–3E). Sedimentary pyrite $\delta^{34}S$ varies widely between locations and stratigraphic horizons, and most of our samples are isotopically heavy (Figs. 3A–3C and 3E versus Fig. 3D; Table S1). Many of our depth profiles through sedimentary pyrite grain cores generated smooth plateaus (representative depth profiles in Figures 3A–3C, resulting in plateau data points shown in Figure 4). Several showed

[1]Supplemental Material. Detailed methods, description of materials, and data tables. Please visit https://doi.org/10.1130/GEOL.S.19175891 to access the supplemental material, and contact editing@geosociety.org with any questions.

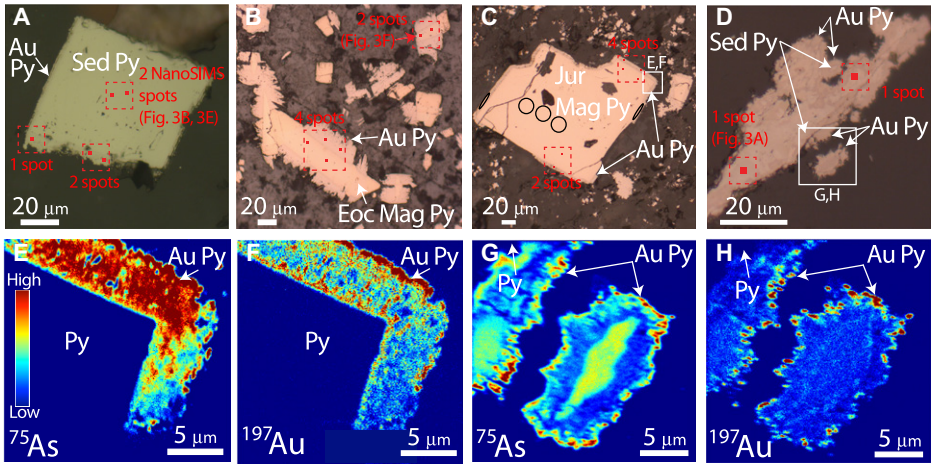

Figure 2. Hydrothermal Carlin-type pyrite overgrowing precursor pyrite. Nanoscale secondary ion mass spectrometry (NanoSIMS) spots are shown to scale as red-filled squares (within larger dashed boxes), laser ablation–multicollector–inductively coupled plasma mass spectrometry (LA-MC-ICPMS) spots as black circles. A–D are reflected light microscopy images. (A) Sedimentary pyrite with Au-As rim from Getchell. (B) Eocene magmatic pyrite from Beast dike with Au-As rim. (C) Jurassic magmatic-hydrothermal pyrite from Deep Star with Au-As rim. (D) Sedimentary pyrite from Turquoise Ridge with complex Au-As overgrowth. (E–H) NanoSIMS trace element maps from white boxes in C (E,F) and D (G,H). Sed—sedimentary; Py—pyrite; Eoc—Eocene; Mag—magmatic-hydrothermal; Jur—Jurassic.

heterogeneity in $\delta^{34}S$ (Figs. 3D and 3E), perhaps due to fluctuations in microbial activity during sedimentary pyrite formation.

The unmineralized Jurassic magmatic-hydrothermal pyrite grain cores from Deep Star contain minor Au and $\delta^{34}S$ values of 6.5‰–6.9‰ (Fig. 4D), close to the mean $\delta^{34}S$ of Jurassic magmatic sulfur in the Great Basin (Arehart et al., 2013). The Eocene magmatic pyrites at Betze-Post, Deep Star, and Beast contain minor Au with $\delta^{34}S$ values (Fig. 4D) within the range of Tertiary magmatic sulfur in the Great Basin, which is itself isotopically variable due to variable host-rock interaction (Fig. 4F).

The NanoSIMS maps and depth profiles show a sharp contact between the precursor pyrite cores and the Au-As–rich hydrothermal rims (Figs. 2 and 3). The Au concentrations vary within the rims at a finer scale than previously surmised (Cline et al., 2005; Barker et al., 2009; Muntean et al., 2011; Large and Maslennikov, 2020) and also vary widely between samples (Figs. 3 and 4). In most samples, the depth profiles also show a dramatic change in $\delta^{34}S$ at the contact between precursor cores and hydrothermal rims (Fig. 3). Within the rims, the $\delta^{34}S$ values commonly vary inversely with Au (Figs. 3 and 4A–4C) but lack correlation with As. The lowest plateau values from the rims come from Au-rich zones: 1.7‰ $\delta^{34}S$ at Getchell, 2.5‰ at Carlin, 1.2‰ at Turquoise Ridge, 4.2‰ at Deep Star, and 2.1‰ at Beast (Figs. 4A–4D).

Two Fluids Contributed to Ore Pyrite Formation

At each deposit, the $\delta^{34}S$ plateau values from the rims plot on a mixing line between two end members (Figs. 4A–4E): (1) an Au-poor sulfur source isotopically similar to local host pyrite cores, and (2) an Au-rich sulfur source with $\delta^{34}S$ values similar to those of mineralizing Eocene magmatic-hydrothermal fluids in the nearby Battle Mountain district (−1.8‰ to 7‰; Fig. 4F) and similar to the mean $\delta^{34}S$ of Great Basin Tertiary granitoid magmas (7.1‰; Arehart et al., 2013). Our microanalytical evidence for two-component mixing is supported by whole-rock geochemical data from Betze-Post's Screamer ore body (Fig. 4D; Christiansen et al., 2011): isotopically variable host pyrite in the Popovich Formation controls the $\delta^{34}S$ values in samples without detectable gold, and a sulfur

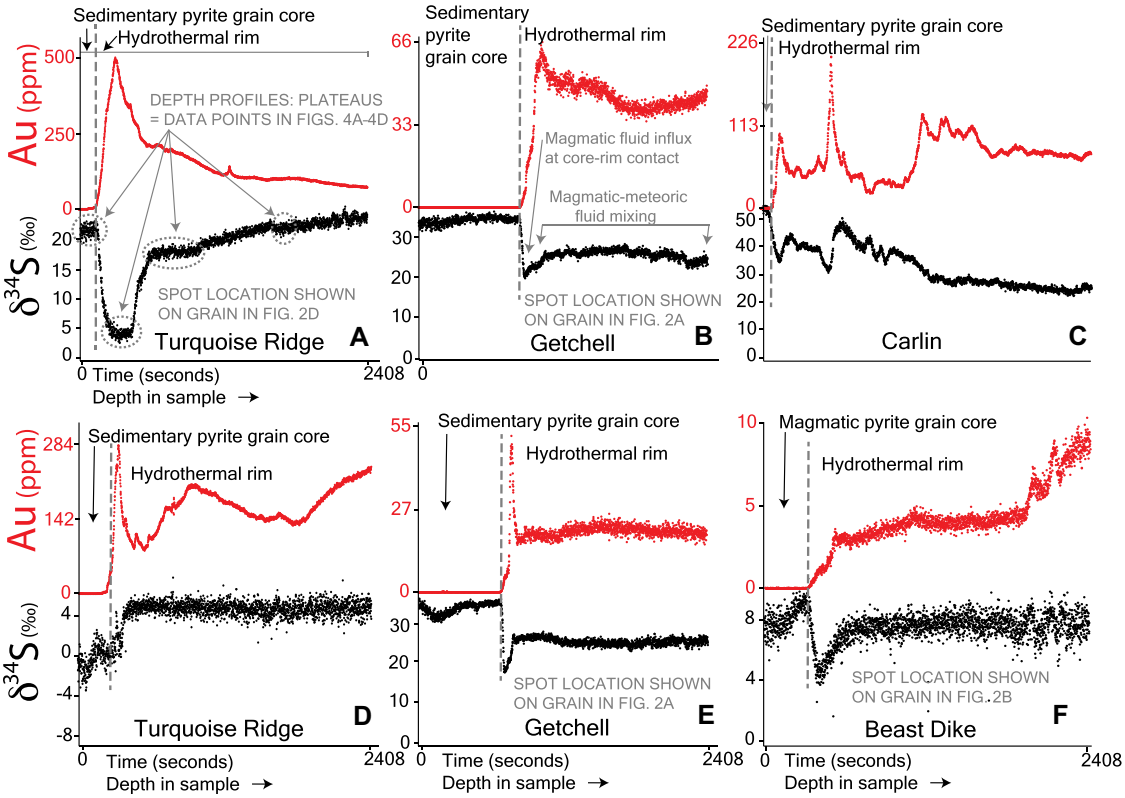

Figure 3. Depth profiles from representative nanoscale secondary ion mass spectrometry (NanoSIMS) analyses of simultaneously detected $\delta^{34}S$ (black) and Au (red), selected from 64 similar analyses of Carlin-type pyrite grains. Vertical lines indicate core-rim boundary.

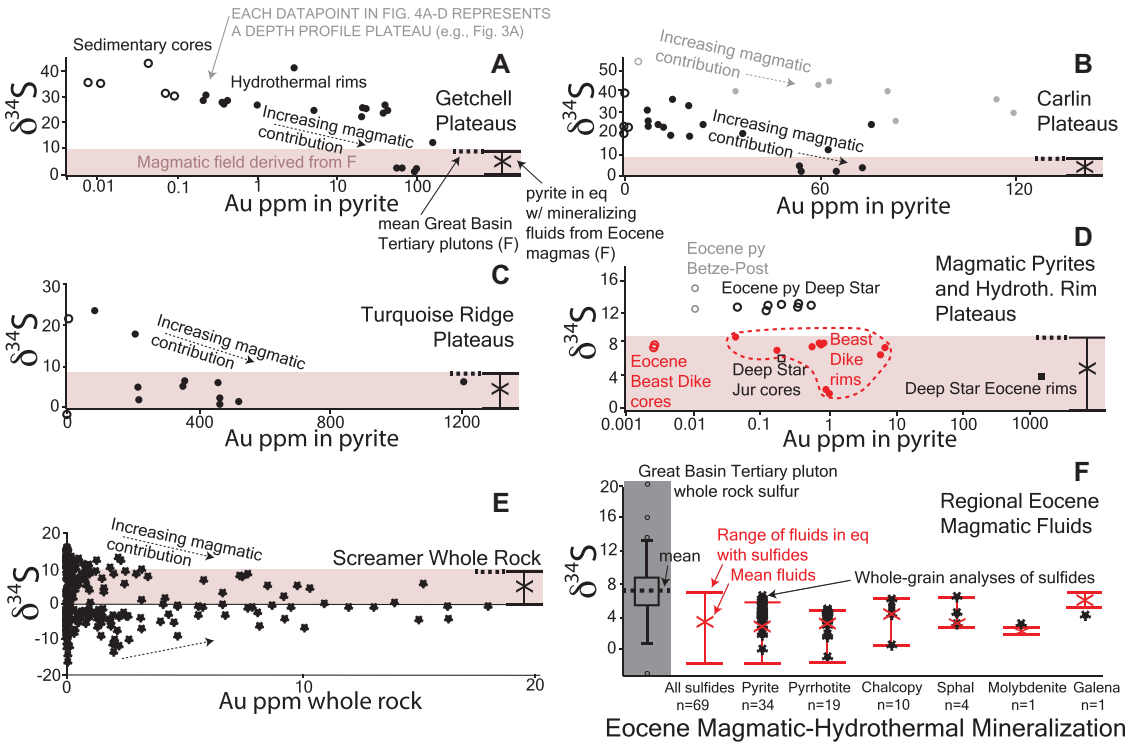

Figure 4. (A–D) Plateaus from nanoscale secondary ion mass spectrometry (NanoSIMS) depth profiles; each data point represents a zone of consistent composition. Open symbols show precursor grain cores; closed symbols are hydrothermal rims. (A–C) Sedimentary pyrite cores and hydrothermal rims at Getchell (A), Carlin (B), and (C) Turquoise Ridge. Gray symbols in B are analyses of individual isotopically heavy grain which itself shows same mixing trend. (D) Magmatic pyrite cores at Betze-Post, Beast, and Deep Star, and hydrothermal rims at Deep Star and Beast. (E) Whole-rock δ^{34}S and Au from Screamer sector of Betze-Post (Christiansen et al., 2011). (F) Box plot of δ^{34}S of Tertiary pluton sulfur in Great Basin (gray; Arehart et al., 2013), Eocene Battle Mountain district porphyry- and pluton-proximal sulfide whole-grain δ^{34}S (black stars; this study; Theodore et al., 1986; King, 2017; Holley et al., 2019), and range of fluids in equilibrium with those sulfide minerals (red whisker plots) (see Methods and Table S3 [see footnote 1]). The δ^{34}S of pyrite that would have precipitated from Eocene magmatic and magmatic-hydrothermal fluids at 200 °C is shown in shaded boxes in A–E.

source near 0‰ contributes substantially at high ore grades. The depth profiles show nanoscale zonation resulting from variation in relative contributions of the two sources over time (Fig. 3).

DISCUSSION

The Au-poor sulfur source may represent dissolution of sulfur-bearing minerals and organosulfur complexes during meteoric fluid circulation through the sedimentary host-rock package. The Au-rich sulfur requires an alternate source to explain the strong correlations between δ^{34}S and Au. A meteoric fluid convecting deeply through sedimentary rock would achieve δ^{34}S compositions representing regional or local averages of the stratigraphy. Although such a fluid could become Au rich by interacting with large volumes of rock containing trace metals or during passage through metalliferous sedimentary horizons (e.g., Large et al., 2011), initial correlations between δ^{34}S and metal content at a mutual point of origin would be lost during fluid circulation due to interaction with isotopically varied sulfur elsewhere in the rock package.

The Au-rich sulfur in Carlin-type ore was most likely derived from Eocene magmas. Magmatic-hydrothermal sulfide minerals from the nearest Eocene porphyry and other pluton-proximal deposits in the Battle Mountain district have δ^{34}S values ranging from −1.0‰ to 6.6‰ (this study; Theodore et al., 1986; King, 2017; Holley et al., 2019). Using a range of realistic precipitation temperatures, the δ^{34}S of the causative Eocene magmatic fluids can be constrained to −1.8‰ to 7.0‰ (Table S3). Temperature-induced fractionation would cause those fluids to precipitate Carlin-type pyrite with a δ^{34}S of 0.0‰–8.8‰ at 200 °C (a reasonable temperature estimate for Carlin-type mineralization; Cline et al., 2005). Because the Au-rich zones of our pyrites gave δ^{34}S values in this range (Figs. 4A–4D), we attribute their origins to the Eocene magmatic fluid.

The causative magmas were isotopically similar to those that generated the Beast dike (δ^{34}S depth profile values of 2.1‰–8.5‰). Eocene magmas of similar compositions either stalled out at depth beneath the Getchell trend or remain unrecognized. During magma cooling, Au and As would have become enriched in the exsolving fluids. Circulation of these fluids in the magmatic-hydrothermal environment led to variable interaction with Au-poor meteoric fluids and other sulfur sources, including isotopically heavy and light sedimentary sulfur minerals, as well as older magmatic and magmatic-hydrothermal sulfur and metals. Upon reaching favorable lithologic horizons and hydrologic or structural traps, these mixing fluids encountered preexisting pyrite. Sulfidation led to hydrothermal pyrite precipitation, and temporal fluctuations in the relative contribution of Au-rich magmatic and Au-poor meteoric fluids led to sequential nanoscale zones with covarying Au and δ^{34}S.

CONCLUSIONS

Carlin-type pyrite provides insights into the processes driving the formation of giant ore deposits. Fluid mixing led to fluctuations in metal precipitation, although the time scales over which the relative fluid contributions varied are unknown. These repeated oscillations were essential in upgrading metal concentrations at the mineral scale, ultimately leading to the formation of world-class ore bodies. In the absence of nanoscale data, previously developed models for metal enrichment in these deposits were overly simplistic, and such models require reevaluation (e.g., Sillitoe and Bonham, 1990; Ilchik and Barton, 1997; Emsbo et al., 2003; Ressel and Henry, 2006; Large et al., 2011; Muntean et al., 2011; Kusebauch et al., 2019; Xing et al., 2019). Low-spatial-resolution analytical methods have been applied to ore deposits for decades, even where micron- to submicron-scale trace element zonation or mineral intergrowths are visible in reflected light microscopy or scanning electron backscatter imaging. Such textures give intriguing hints that fluid mixing played a key role during mineralization in numerous geological settings, and our study highlights how high-spatial-resolution observations can elucidate the underlying geological processes.

ACKNOWLEDGMENTS

This study was funded by U.S. National Science Foundation (NSF) Career Award EAR-1752756 (E.A. Holley). The Stanford Nano Shared Facilities are

supported by NSF award ECCS-2026822. We thank Jean Cline, Phillip Gopon, Al Hofstra, Mike Ressel, and Patrick Sack for samples and discussion; Aaron Bell, Nigel Kelly, and Katharina Pfaff for analyses; Jae Erickson, Kelsey Livingston, Sage Langston-Stewart, and Heather Lowers for sample preparation; and Chris Henry, Celestine Mercer, Adam Simon, and an anonymous reviewer for comments. Any use of trade, firm, or product names is for descriptive purposes only and does not imply endorsement by the U.S. Government.

REFERENCES CITED

Arehart, G.B., DeYoung, S., Poulson, S.R., Heaton, J.S., and Weiss, S., 2013, Sulfur isotopes in plutonic rocks of the Great Basin as indicators of crustal architecture: The Journal of Geology, v. 121, p. 355–369, https://doi.org/10.1086/670651.

Barker, S.L.L., Hickey, K.A., Cline, J.S., Dipple, G.M., Kilburn, M.R., Vaughan, J.R., and Longo, A.A., 2009, Uncloaking invisible gold: Use of nanoSIMS to evaluate gold, trace elements, and sulfur isotopes in pyrite from Carlin-type gold deposits: Economic Geology, v. 104, p. 897–904, https://doi.org/10.2113/econgeo.104.7.897.

Christiansen, W.D., Hofstra, A.H., Zohar, P.B., and Tousignant, G., 2011, Geochemical and stable isotopic data on barren and mineralized drill core in the Devonian Popovich Formation, Screamer sector of the Betze-Post gold deposit, northern Carlin trend, Nevada: U.S. Geological Survey Open-File Report 2010-1077, 11 p., https://doi.org/10.3133/ofr20101077.

Cline, J.S., 2018, Nevada's Carlin-type gold deposits: What we've learned during the past 10 to 15 years, ***in*** Muntean, J.L., ed., Diversity in Carlin-Style Gold Deposits: Society of Economic Geologists Reviews in Economic Geology 20, p. 7–37, https://doi.org/10.5382/rev.20.01.

Cline, J.S., Stuart, F.M., Hofstra, A.H., Premo, W., Riciputi, L., Tosdal, R.M., and Tretbar, D.R., 2003, Multiple sources of ore-fluid components at the Getchell Carlin-type gold deposit, Nevada, USA, *in* Eliopoulos, D.G., ed., Mineral Exploration and Sustainable Development: Proceedings of the Seventh Biennial SGA Meeting on Mineral Exploration and Sustainable Development, Athens, Greece, August 24–28, 2003: Rotterdam, Millpress, p. 965–968.

Cline, J.S., Hofstra, A.H., Muntean, J.L., Tosdal, R.M. and Hickey, K.A., 2005, Carlin-type gold deposits in Nevada: Critical geologic characteristics and viable models, *in* Hedenquist, J.W., et al., eds., Economic Geology One Hundredth Anniversary Volume: 1905–2005: Littleton, Colorado, Society of Economic Geologists, p. 451–484, https://doi.org/10.5382/AV100.15.

Emsbo, P., Hofstra, A.H., Lauha, E.A., Griffin, G.L., and Hutchinson, R.W., 2003, Origin of high-grade gold ore, source of ore fluid components, and genesis of the Meikle and neighboring Carlin-type deposits, northern Carlin trend, Nevada: Economic Geology, v. 98, p. 1069–1105, https://doi.org/10.2113/gsecongeo.98.6.1069.

Goldfarb, R.J., Hofstra, A.H., and Simmons, S.F., 2016, Critical elements in Carlin, epithermal, and orogenic gold deposits, *in* Verplanck, P.L., and Hitzman, M.W., eds., Rare Earth and Critical Elements in Ore Deposits: Society of Economic Geologists Reviews in Economic Geology 18, p. 217–244, https://doi.org/10.5382/Rev.18.10.

Gopon, P., Douglas, J.O., Auger, M.A., Hansen, L., Wade, J., Cline, J.S., Robb, L.J., and Moody, M.P., 2019, A nanoscale investigation of Carlin-type gold deposits: An atom-scale elemental and isotopic perspective: Economic Geology, v. 114, p. 1123–1133, https://doi.org/10.5382/econgeo.4676.

Harper, J., 2020, How much gold is there left to mine in the world?: BBC News, 23 September 2020, https://www.bbc.com/news/business-54230737.

Hauri, E.H., Papineau, D., Wang, J., and Hillion, F., 2016, High-precision analysis of multiple sulfur isotopes using NanoSIMS: Chemical Geology, v. 420, p. 148–161, https://doi.org/10.1016/j.chemgeo.2015.11.013.

Henkelman, C.A., 2004, Pyrite geochemistry across the Betze-Post deposit, northern Carlin Trend, Nevada [Ph.D. thesis]: Las Vegas, University of Nevada, 163 p.

Henry, C.D., and John, D.A., 2013, Magmatism, ash-flow tuffs, and calderas of the ignimbrite flareup in the western Nevada volcanic field, Great Basin, USA: Geosphere, v. 9, p. 951–1008, https://doi.org/10.1130/GES00867.1.

Henry, C.D., John, D.A., Leonardson, R.W., McIntosh, W.C., Heizler, M.T., Colgan, J.P., and Watts, K.E., 2021, Timing of rhyolite intrusion and Carlin-type gold mineralization at the Cortez Hills Carlin-type deposit, Nevada, USA: Economic Geology (in press).

Hofstra, A.H., and Cline, J.S., 2000, Characteristics and models for Carlin-type gold deposits, *in* Hagemann, S.G., and Brown, P.E., eds., Gold in 2000: Society of Economic Geologists Reviews in Economic Geology 13, p. 163–220, https://doi.org/10.5382/Rev.13.05.

Holley, E.A., Lowe, J.A., Johnson, C.A., and Pribil, M.J., 2019, Magmatic-hydrothermal gold mineralization at the Lone Tree mine, Battle Mountain District, Nevada: Economic Geology, v. 114, p. 811–856, https://doi.org/10.5382/econgeo.4665.

Ilchik, R.P., and Barton, M.D., 1997, An amagmatic origin of Carlin-type gold deposits: Economic Geology, v. 92, p. 269–288, https://doi.org/10.2113/gsecongeo.92.3.269.

Kesler, S.E., Ye, Z., Fortuna, J., and Riciputi, L.C., 2003, Epithermal Carlin transition: Evidence for magmatic input to Carlin-type deposits, *in* Eliopoulos, D.G., ed., Mineral Exploration and Sustainable Development: Proceedings of the Seventh Biennial SGA Meeting on Mineral Exploration and Sustainable Development, Athens, Greece, August 24–28, 2003: Rotterdam, Millpress, p. 493–494.

Kesler, S.E., Riciputi, L.C., and Ye, Z., 2005, Evidence for a magmatic origin for Carlin-type gold deposits: Isotopic composition of sulfur in the Betze-Post-Screamer Deposit, Nevada, USA: Mineralium Deposita, v. 40, p. 127–136, https://doi.org/10.1007/s00126-005-0477-9.

King, C.A., 2017, Igneous petrology, geochronology, alteration, and mineralization associated with hydrothermal systems in the Battle Mountain district, Nevada [Ph.D. thesis]: Tucson, University of Arizona, 707 p.

Kusebauch, C., Gleeson, S.A., and Oelze, M., 2019, Coupled partitioning of Au and As into pyrite controls formation of giant Au deposits: Science Advances, v. 5, eaav5891, https://doi.org/10.1126/sciadv.aav5891.

Large, R.R., and Maslennikov, V.V., 2020, Invisible gold paragenesis and geochemistry in pyrite from orogenic and sediment-hosted gold deposits: Minerals (Basel), v. 10, p. 339–360, https://doi.org/10.3390/min10040339.

Large, R.R., et al., 2009, Gold and trace element zonation in pyrite using a laser imaging technique: Implications for the timing of gold in orogenic and Carlin-style sediment-hosted deposits: Economic Geology, v. 104, p. 635–668, https://doi.org/10.2113/gsecongeo.104.5.635.

Large, R.R., Bull, S.W., and Maslennikov, V.V., 2011, A carbonaceous sedimentary source-rock model for Carlin-type and orogenic gold deposits: Economic Geology, v. 106, p. 331–358, https://doi.org/10.2113/econgeo.106.3.331.

Muntean, J.L., Cline, J.S., Simon, A.C., and Longo, A.A., 2011, Magmatic-hydrothermal origin of Nevada's Carlin-type gold deposits: Nature Geoscience, v. 4, p. 122–127, https://doi.org/10.1038/ngeo1064.

Nevada Gold Mines, 2021, Nevada Gold Mines May 2021 Investor Day: https://s25.q4cdn.com/322814910/files/doc_presentations/2021/NGM_Investor_Day_03_Exploration_MRM.pdf (accessed December 29021).

Pinet, N., Sack, P., Mercier-Langevin, P., Colpron, M., Lavoie, D., Dubé, B., and Brake, V.I., 2020, Neoproterozoic-hosted Carlin-type mineralization in central Yukon, part 1: Regional- to prospect-scale geological controls, ***in*** Mercier-Langevin, P., et al., eds., Targeted Geoscience Initiative 5: Contributions to the Understanding of Canadian Gold Systems: Geological Survey of Canada Open File Report 8712, p. 281–297, https://doi.org/10.4095/326045.

Ressel, M.W., and Henry, C.D., 2006, Igneous geology of the Carlin trend, Nevada: Development of the Eocene plutonic complex and significance for Carlin-type gold deposits: Economic Geology, v. 101, p. 347–383, https://doi.org/10.2113/gsecongeo.101.2.347.

Richards, J.P., 2011, Hidden gold: Nature Geoscience, v. 4, p. 73–74, https://doi.org/10.1038/ngeo1072.

Sillitoe, R.H., and Bonham, H.F., Jr., 1990, Sediment-hosted gold deposits: Distal products of magmatic-hydrothermal systems: Geology, v. 18, p. 157–161, https://doi.org/10.1130/0091-7613(1990)018<157:SHGDDP>2.3.CO;2.

Theodore, T.G., Howe, S.S., Blake, D.W., and Wotruba, P.R., 1986, Geochemical and fluid zonation in the skarn environment at the Tomboy-Minnie gold deposits, Lander County, Nevada: Journal of Geochemical Exploration, v. 25, p. 99–128, https://doi.org/10.1016/0375-6742(86)90009-9.

Wallace, A.R., et al., 2004, Assessment of Metallic Mineral Resources in the Humboldt River Basin, Northern Nevada: U.S. Geological Survey Bulletin 2218, 309 p., https://pubs.usgs.gov/bul/b2218/.

Xing, Y., Brugger, J., Tomkins, A., and Shvarov, Y., 2019, Arsenic evolution as a tool for understanding formation of pyritic gold ores: Geology, v. 47, p. 335–338, https://doi.org/10.1130/G45708.1.

Zhang, J., Lin, Y., Yang, W., Shen, W., Hao, J., Hu, S., and Cao, M., 2014, Improved precision and spatial resolution of sulfur isotope analysis using NanoSIMS: Journal of Analytical Atomic Spectrometry, v. 29, p. 1934–1943, https://doi.org/10.1039/C4JA00140K.

Zhang, J., Lin, Y., Yan, J., Li, J., and Yang, W., 2017, Simultaneous determination of sulfur isotopes and trace elements in pyrite with a NanoSIMS 50L: Analytical Methods, v. 9, p. 6653–6661, https://doi.org/10.1039/C7AY01440F.

Printed in USA